INORGANIC CHEMISTRY FRONTIERS

RESEARCH ARTICLE

View Article Online
View Journal

Cite this: DOI: 10.1039/d5qi02453f

Tailored polyMOFs for ion transport in lithium-based battery electrolyte

Ian J. Dillingham,[a] Vibhu Vardhan Singh,[b,c] Rebecca Y. Han,[a] Liwen F. Wan *[c] and V. Sara Thoi *[a,d]

Owing to their low flammability, solid-state and quasi-solid-state electrolytes are safer alternatives to liquid organic electrolytes for energy storage applications. Metal–organic frameworks (MOFs), with facile functional tunability, long-range order, and rich host–guest interactions, have been implemented as electrolyte materials in a wide range of energy storage applications. In this work, we investigate a class of MOFs called polyMOFs as quasi-solid-state electrolyte materials. Unlike MOF–polymer composites, which are physical mixtures of MOF particles and polymers, polyMOFs are composed of polymeric linkers and metal ion nodes that self-assembled into crystalline and porous framework materials. PolyMOFs thus marry the ionic transport properties of liquid electrolyte and polymers with the synthetic versatility and host–guest interactions of MOFs. We demonstrate that the functionality of the polymer backbone of the polyMOF linker can improve room-temperature ion transport in the material. The polyMOF based on poly(ethylene glycol) (PEG) exhibits greater ionic conductivity, lithium transference number, and lower activation energy than its polyethylene (PE) analog. Supported by solid-state ^{7}Li nuclear magnetic resonance spectroscopy, we propose these improvements are due to stronger coordination of Li^{+} to oxide sites in PEG, allowing for dissociation of Li and its associated anion. DFT studies further reveal that the confined solvent molecule mediates Li^{+} transport in PEG-functionalized UiO-66 *via* a metastable adsorption and hopping mechanism. This work lies at the interface of inorganic and polymer electrolytes, unveiling fundamental insights into the design of next-generation ion conductive materials for energy technologies.

Received 3rd December 2025,
Accepted 1st April 2026

DOI: 10.1039/d5qi02453f

rsc.li/frontiers-inorganic

Introduction

Solid-state batteries are promising candidates for high-capacity energy storage solutions for advanced electronics, electric vehicles, and large-scale stationary storage technology. By utilizing solid-state electrolytes (SSEs), energy density can be increased while mitigating flammability risks and possible release of volatile and toxic electrolyte.[1,2] However, SSEs suffer from low ionic conductivity, mechanical and chemical instability, and high interfacial resistance.[3–5] Solid polymer electrolytes (SPEs) have the potential to solve many of these issues in traditional inorganic SSEs.[6–9] Containing a mixture of polymer and lithium salt, SPEs offer facile processability for fabrication into electrolyte separators, as well as mechanical stability and relatively high flexibility. They are also inexpensive to manufacture due to the availability of polymer feedstocks and lithium salts.[10]

A well-established SPE is polyethylene glycol (PEG, also referred to as poly(ethylene oxide) or PEO), which contains oxide sites along the polymer chain that allow for hopping of Li^{+}.[11] However, PEG has low room-temperature ionic conductivity (on the order of 10^{-7}–10^{-8} S cm^{-1})[12] due to the presence of crystalline phase domains, requiring elevated temperatures (typically >70 °C) for cell operation.[13] Like many polymer electrolytes, PEG typically require a filler to reduce the number of crystalline phase domains.[8] This strategy can increase the mechanical and ionic properties of the material, but heterogeneous dispersion and insufficient ion conduction pathways in the filler can lead to undesirable internal resistances. Examples of common fillers for PEG-based SPEs include succinonitrile, low-molecular weight polymers, ceramic metal-oxides, and porous metal–organic materials.[9,14,15]

Metal–organic frameworks (MOFs) are organic–inorganic hybrid materials that boast high specific surface area, chemical tunability, and ordered micro-/meso-porous channels.[16]

[a]Department of Chemistry, Johns Hopkins University, Baltimore, Maryland 21218, USA. E-mail: sarathoi@jhu.edu
[b]Aiiso Yunfeng Li Family of Chemical and Nano Engineering, University of California San Diego, La Jolla, CA 92093, USA
[c]Laboratory for Energy Applications for the Future, Lawrence Livermore National Laboratory, Livermore, California 94550, USA. E-mail: wan6@llnl.gov
[d]Department of Materials Science and Engineering, Johns Hopkins University, Baltimore, Maryland 21218, USA

MOFs are often used in battery research as electrode additives as well as SSEs and quasi-solid-state electrolytes (QSSEs).[17,18] Quasi-solid-state electrolytes (QSSEs) have garnered attention recently for their ability to leverage improved ionic conductivity in a solid-state form factor. QSSEs differ from SSEs in that they contain a small amount of liquid electrolyte within the solid material to improve the ionic conductivity and interfacial resistance.[19] For instance, quasi-solid-state SPEs are formed by soaking the polymeric membrane in a liquid electrolyte or through an *in situ* polymerization process in an electrolyte solution.[20,21] MOF-based QSSEs are formed by infiltrating the pores of the MOFs with a liquid electrolyte.[22,23] Because of their micropores, MOFs absorb ions and solvent molecules, harnessing the ionic transport of liquid electrolyte while retaining solid-state physical properties and processability. Previously, Shen *et al.* functionalized the open metal sites of MOFs with perchlorate anions that promoted ion hopping along the framework channels.[24,25] MOFs can also serve as fillers and plasticizers for quasi-solid-state SPEs to act as a host for liquid electrolyte and disassociate Li salts for improved conductivity.[26] For instance, UiO-66-NH_2 was incorporated into solid polymer electrolytes as a filler to reduce dendrite growth.[27] The MOF can increased the ionic conductivity of the SPEs due to its polar functional groups, which caused interruption of insulating crystalline PEG phases.[8,14,27]

While there has been a plethora of research focused on the interplay of MOFs and polymers in QSSE and SSEs, most studies treat the two materials as distinct components, either physically mixing MOF and polymer into a composite membrane, or through grafting MOF particles together through post-synthetic surface polymerization.[26,28,29] In this study, we leverage the coordination sites of PEG and the tunability of framework materials in a class of MOFs called polyMOFs as a hybrid inorganic polymer electrolyte. Originally pioneered by Cohen and coworkers, polyMOFs utilize polymeric linkers (denoted as polylinkers) containing repeated units of a flexible polymeric chain and a rigid organic component for binding the metal ions.[30–33] Notably, polylinkers are synthesized prior to solvothermal assembly in polyMOFs, an important distinction from MOFs that are post-synthetically decorated with polymeric groups. This synthetic strategy assures uniform distribution of the polymeric component in the framework and reduces the likelihood of incomplete functionalization of the linkers. PolyMOFs are also unique from MOF–polymer composite electrolytes. In these physically-mixed composite systems, the ion transport properties are dominated by the polymer and the MOF serves secondary roles, such as providing structural support or as a filler material to disrupt insulating crystalline phases. In contrast, polyMOFs are designed for both ion transport and mechanical rigidity. As the polymeric chains are inherently interrupted by the metal nodes, polyMOFs have the advantage of preventing the formation of insulating crystalline polymer phases that are typical in polymer matrices.[34]

Herein, we synthesized a novel UiO-66 polyMOF with a PEG-containing polylinker (polyUiO-66-PEG) and compared its ion transport properties with a polyethylene-based analog (polyUiO-66-PE).[30] Infiltration of $LiClO_4$ and propylene carbonate (PC) into the polyMOFs generated a QSSE, where PC molecules and Li salts are trapped in the pores. The polyUiO-66-PEG QSSE exhibits a relatively high pellet ionic conductivity of 7.2×10^{-5} S cm^{-1} compared to polyUiO-66-PE (3.0×10^{-5} S cm^{-1}) at room temperature. Solid-state ^{7}Li nuclear magnetic resonance (NMR) spectroscopy and density functional theory (DFT) were used to further probe the local Li^+ environment, revealing possible Li^+ coordination with oxide sites and embedded PC molecules in UiO-66-PEG. Collectively, our results illustrate the potency in leveraging the tunability of MOFs to design ion transport pathways conventionally established for solid polymer electrolytes.

Experimental

Materials

Diethyl 2,5-dihydroxyterephthalate (98%, Combi-Blocks), 1,7-dibromoheptane (97%, Sigma-Aldrich), potassium carbonate (≥ 99%, Alfa-Aesar), *N*,*N*-dimethylformamide (DMF, ACS grade, Sigma-Aldrich), potassium hydroxide pellets (KOH, 85%, Thermo Scientific), hydrochloric acid (HCl, ACS grade, Sigma-Aldrich), acetone (ACS grade, Pharmco), methanol (CH_3OH, HPLC grade, Sigma-Aldrich), chloroform (CH_3Cl, ACS certified, Fisher Chemical), triethylene glycol (99.9%+, Sigma-Aldrich), pyridine (99.9%, Sigma-Aldrich), *p*-toluenesulfonyl chloride (≥99%, Sigma-Aldrich). Sodium bicarbonate ($NaHCO_3$, anhydrous, ≥99.7%, Sigma Aldrich), zirconium(IV) chloride ($ZrCl_4$, anhydrous, Sigma-Aldrich), diethyl formamide (DEF, 99.98%, Ambeed), formic acid (99%, Thermo Scientific), lithium perchlorate ($LiClO_4$, 99.99% trace metal basis, Sigma-Aldrich), lithium bis(trifluoromethanesulfonyl)imide (LiTFSI, Oakwood Chemical, 99%), 1,3-dioxolane (DOL, Acros Organics), 1,2-dimethoxyethane (DME, Alfa Aesar), and propylene carbonate (PC, anhydrous 99.7%, Sigma-Aldrich) were used without further purification. Anhydrous diethyl ether (Et_2O) was purified through an Innovative Technology Solvent Purification System before usage. DMSO-d^6 (99.9%) and chloroform-d (99.8%) were purchased from Cambridge Isotope Labs. Lithium chips, 16 mm diameter, 0.6 mm thickness, were purchased from Vivtek.

Instrumentation

Powder X-ray diffraction was conducted on a Bruker D8 Focus diffractometer with LynxEye detector and Cu Kα radiation (PXRD). Liquid-phase nuclear magnetic resonance (NMR) measurements were done using a Bruker Avance 400 MHz spectrometer while solid-state NMR was conducted on a Bruker 500 MHz spectrometer. Electrochemical impedance spectroscopy (EIS) and potentiostatic polarization experiments were done on a Gamry Reference 600+ potentiostat. Thermogravametric analysis (TGA) was conducted on a TA Instruments SDT-Q600. Scanning electron microscopy (SEM) were captured on a JSM-IT700HR InTouchScope Field Emission. Atomic absorption spectroscopy (AAS) was done on

an Agilent 240FS AA instrument with an Agilent Li hollow cathode lamp after complete dissolution of samples in H_2SO_4 for 12 h and using a standard calibration curve.

Polymer molecular weights were measured by gel permeation chromatography (GPC) on a Tosoh Bioscience EcoSEC GPC workstation, using butylated hydroxytoluene stabilized tetrahydrofuran (THF) as the eluent (0.35 mL min^{-1}, 40 °C) through TSKgel SuperMultipore HZ-M guard column (4.6 mm ID × 2.0 cm, 4 μm, Tosoh Bioscience) and a TSKgel SuperMultipore HZ-M column (4.6 mm ID × 15 cm, 4 μm, Tosoh Bioscience). Polystyrene standards (EasiVial PS-M, Agilent) were used to build a calibration curve. Processing was performed using EcoSEC Data Analysis software (Version 1.14, Tosoh Bioscience). Polymers were dissolved in THF (1 mg mL^{-1}), filtered (Millex-FG Syringe Filter Unit, 0.20 μm, PTFE, EMD Millipore), and injected using an auto-sampler (10 μL).

Synthesis of poly[(benzenedicarboxylic acid)-*co*-heptane] (pbdc-7PE)

The procedure was adapted from Cohen *et al.*[30] Diethyl 2,5-dihydroxyterephthalate (2.2 g, 8.7 mmol), 1,7-dibromoheptane (2.2 g, 8.7 mmol), and potassium carbonate (4.8 g, 34.4 mmol) are added to 55 mL of *N*,*N*-dimethylformamide (DMF) and stirred. The suspended mixture was heated at 100 °C for 24 h. The mixture was cooled and precipitated out into DI water dropwise. The polymer was isolated by centrifugation at 8000 rpm for 15 minutes. The solid material was redissolved in DMF and reprecipitated into water 3 times before being washed with acetone and methanol, each in triplicate. Solids were then dried at 60 °C overnight. Ester groups were hydrolyzed by placing the protected polylinker (1.6 g, 4.5 mmol) and potassium hydroxide (6.4 g, 114.1 mmol) in a 15 mL DMF and 15 mL DI water mixture. The mixture was heated to 80 °C for 16 h until the solution was clear. 1.0 M HCl was added until the solution reached a pH of ~2, and then solids were collected by centrifugation. Polymers were then washed with acetone and methanol, each in triplicate. Off-white solids were dried at 60 °C overnight (45–55% yield). ^{1}H-NMR (400 MHz, DMSO-d6): δ 7.26 (s, 2H), 3.98 (t, J = 6.1 Hz, 4H); 1.69 (t, J = 6.0 Hz, 4H), 1.49–1.31 (m, 6H).

Synthesis of triethylene glycol *p*-tolunenesulfonate

30 mL of chloroform was chilled to 0 °C in a 3-neck 100 mL round bottom flask. Triethylene glycol (6.0 g, 40.0 mmol), and pyridine (9.7 mL, 9.5 g, 120 mmol) is added. The mixture was stirred until homogeneous. An addition funnel was attached to the round bottom flask, and *p*-toluenesulfonyl chloride (17.2 g, 90 mmol) dissolved in minimal chloroform (10–20 mL) was added. The mixture was slowly added dropwise to flask under nitrogen atmosphere. Once completely added, the reaction was allowed to proceed until complete, taking about 1 h. After reacting, 1.0 M NaOH solution and diethyl ether were added (bringing volume to ~100 mL). The solution was washed with HCl, $NaHCO_3$, water, and brine. The organic layer was separated, and solvent was removed through rotary evaporation. A white waxy solid appearred within 24 h, with faster crystallization occurring at refrigerated temperatures (70% yield). ^{1}H-NMR (400 MHz, $CDCl_3$): δ 7.79 (d, J = 8.3 Hz, 4H), 7.34 (d, J = 8.0 Hz, 4H); 4.14 (t, J = 4.8 Hz, 4H), 3.65 (t, J = 4.8 Hz, 4H), 3.52 (s, 4H), 2.44 (s, 6H).

Synthesis of poly[(benzenedicarboxylic acid)-*co*-(triethylene glycol)] (pbdc-8PEG)

The procedure was adapted from Cohen *et al.*[30] Diethyl 2,5-dihydroxyterephthalate (5.6 g, 22.0 mmol), triethylene glycol ditosylate (10.1 g, 22.0 mmol), and potassium carbonate (12.2 g, 217.5 mmol) were added to 120 mL of DMF and stirred. The suspended mixture was heated at 100 °C for 24 h. The mixture was cooled and precipitated out into DI water dropwise. The polymer was isolated by centrifugation at 8000 rpm for 15 min. The solid brown material was redissolved in DMF and reprecipitated into water 3 times before being washed with acetone and methanol, each in triplicate. Beige solids were then dried at 60 °C overnight. The yields were roughly ~20%. Ester groups were hydrolyzed by placing the protected polylinker (1.5 g, 4.1 mmol) and potassium hydroxide (6.0 g, 106.9 mmol) in a 40 mL DMF and 30 mL DI water mixture. The mixture was heated to 80 °C for 16 h until the solution was clear. 1.0 M HCl was added until the solution reached a pH of ~2, and then solids were collected by centrifugation. Polymers were then washed with methanol in triplicate. Beige solids were dried at 60 °C overnight (~48%). ^{1}H-NMR (400 MHz, DMSO-d6): δ 7.27 (s, 1H), 4.16 (t, J = 4.4 Hz, 2H); 3.73 (t, J = 4.4 Hz, 2H); 3.61 (s, 1H).

General synthesis of UiO-66 polyMOFs

Procedure was adapted and modified from Cohen *et al.*[35] Polylinker (0.03 mmol) and $ZrCl_4$ (0.37 mmol) were dissolved in 2 mL of DEF in a 20 mL scintillation vial. Once dissolved, 2 mL of formic acid was added to the solution. The sample vial was sealed and heated at 135 °C for 48 h. Once cooled, a powder was collected from the bottom of the vial and separated from the supernatant by centrifugation (8000 rpm, 15 min). The solids were then washed with DEF and acetone, each in triplicate. Beige solids were dried under vacuum at 115 °C for 4 h to remove adsorbed solvents.

Electrochemical measurements

Vacuum-dried polyMOFs were brought into an air-and-moisture free Ar glovebox. The polyMOF powder was soaked in a solution of 1.0 M $LiClO_4$ in PC (or LiTFSI in 1 : 1 by volume of DOL and DME) at a proportion of 3 mL per 100 mg of polyMOF, according to previously reported procedures.[24] The solids were then collected by vacuum filtration, and allowed to sit for 3 h under dynamic vacuum. For EIS measurements, ~20 mg of powder was then pressed with a vise into a 6 mm diameter pellet using a stainless-steel custom-built die, placed between copper foil for electrical connection. The die was wrapped with electrical tape to minimize air and moisture exposure, then the whole assembly was removed from the glovebox for EIS measurements in either a Gamry Faraday Cage or in a Tenney environmental chamber (Fig. S1).

To determine Li^+ transference number, a potentiostatic polarization method called the Bruce–Vincent method was employed from literature.[36,37] Dry Li^+-loaded polyMOFs were pressed into a 8 mm diameter pellet using a hand-operated pellet press and die set. The pellet was then carefully removed from the die and inspected for defects before placing between two lithium metal disks, scraped to remove oxide buildup. The assembly was placed in a cell that affixed the materials between two stainless steel plates, and potentiostat connections were fastened to begin measurements. Potentiostatic polarization measurements (20 mV) were used to determine initial and steady-state current (I_0 and I_{SS}, respectively). Steady-state current was considered after negligible changes for 5 min. Immediately before and after polarization, EIS measurements were taken (10^6 to 0.1 Hz, 20 mV amplitude) to determine the interfacial resistance before and after polarization (R_0 and R_{ss}, respectively). The Li^+ transference number, t_{Li^+}, was calculated by using eqn (S1).

To determine the activation energy, we utilized variable-temperature (VT) EIS. VT-EIS measurements were taken using non-blocking stainless steel electrodes using the previously described EIS cell. Measurements were taken at 15 °C intervals ranging from 25 °C to 70 °C. Ionic conductivities were determined from resistances calculated from a Randles circuit fit, then fit to an Arrhenius-type plot to determine activation energies for long-range diffusion from the slope, as shown in eqn (S2).

We also used variable-temperature solid-state ^{7}Li NMR (VT-SSNMR), as an alternate method for determining activation energy for local molecular motion. This method is based on a paper by J. R. Hendrickson and P. J. Bray, who measure the degree of motional narrowing of NMR peaks for diffusing ions in solid electrolytes as a function of temperature and fit those values to an equation that connects that relationship to the activation energy of the ionic diffusion process.[38] To measure this motional narrowing, we pack a 3.2 mm ZrO_2 SSNMR rotor with polyMOF pre-soaked with electrolyte and dried. We then collect MAS ^{7}Li SSNMR spectra at 10 000 Hz rotation speed at varying temperatures, starting at −30 °C and increasing to 70 °C in 10 °C increments. The full width at half the maximum intensity of the peak is taken and plotted in a linearized form of the Hendrickson and Bray equation to determine the activation energy from the slope (eqn (S3)).

Theory and computation

PolyMOF structures were initially constructed by placing polymer chains across different linker groups using the methods proposed by Mu *et al.*, with possible arrangements as depicted in Fig. 5a.[39] To sample initial configurations of Li-incorporated structures, a classical UFF force field was used to model the polyMOF framework and the OPLS-AA force field parameters were used to represent Li^+, ClO_4^- and PC.[40] Atomic charges were assigned using the cm5 charge population analysis method, with a scaling factor of 0.6 as proposed by Hou *et al.* to correct the often overestimated intermolecular interactions in these non-polarizable force fields.[41,42] The different configurations of Li and PC across a viable connected pathway as shown in Fig. S9 were generated by taking the Li-PC distance as a collective variable and performing classical molecular dynamic (CMD) simulations for 10 ns at 1000 K under NPT ensemble, followed by 10 ns NVT at 500 K, with restraining Li-PC at different distances to sample the configurational space. To maintain charge neutrality of the simulation cell, counter-ion, *i.e.* ClO_4^- was placed in the polyMOF framework, at the tetrahedral site away from Li^+ (>5.5 Å). All CMD simulations were performed using the LAMMPS code. Final configurations obtained from these CMD simulation were relaxed using DFT to calculate their relative energy values. The DFT calculations was performed using the Vienna *ab initio* simulation package (VASP) with the projector augmented-wave (PAW) approach.[43,44] The Perdew–Burke–Ernzerhof form of Generalized Gradient Approximation (GGA) was used to approximate the exchange–correlation effect of electrons.[45] Spin-polarized calculations with energy cutoff of 520 eV and a 1 × 1 × 1 Gamma point *k*-point sampling was applied, with an energy and force relaxation threshold chosen to be 10^{-5} and 0.02 eV Å^{-1}, respectively. All degrees of freedom (simulation cell, shape and positions) were allowed to relax during structure optimization in DFT and final coordination environment of Li^+ is determined by considering its nearest neighbour interaction with oxygen within a distance of 2.3 Å. The accessible volume calculations were performed using the Mercury software with the probe radius value taken equal to the average Li–O distance in these polyMOFs.[46]

Results and discussion

The PEG- and PE-based polylinkers were synthesized using adapted procedures from Cohen *et al.*[30] Briefly, an ethoxide-protected 2,5-dioxido-1,4-benzenedicarboxylate (DOBDC) was reacted with either 1,7-dibromoheptane or triethylene glycol *p*-tolunenesulfonate to form poly(H_2BDC-alt-heptane) and poly(H_2BDC-alt-triethylene glycol), referred to here as pbdc-7PE and pbdc-8PEG, respectively (Scheme 1). The ^{1}H NMR spectra, shown in Fig. S2, confirm the structures of the polylinkers, with expected peak integrations. Gel permeation chromatography (GPC) was used to determine the polymer chain length of pbdc-8PEG (Fig. S3). Results show a M_w of 1744, resulting in ~5 AB units per chain. Due to solubility issues, GPC data was not collected for pbdc-7PE, though the polylinker has been previously reported to have a M_w of 1200 g mol^{-1} and 18 AB units per chain using the same synthetic procedure.[30]

Solvothermal synthesis of the respective polyMOFs was achieved by heating a DEF solution of $ZrCl_4$, the polylinker, and formic acid to 135 °C. Following multiple washing steps, polyUiO-66-PEG and polyUiO-66-PE were characterized by powder X-ray diffraction (PXRD) to assess crystallinity and structure (Fig. 1a). PXRD patterns show excellent crystallinity, with the characteristic two high-angle peaks associated with the structure of UiO-66.[47] Scanning electron microscopy (SEM) images of polyUiO-66-PEG and polyUiO-66-PE are shown in

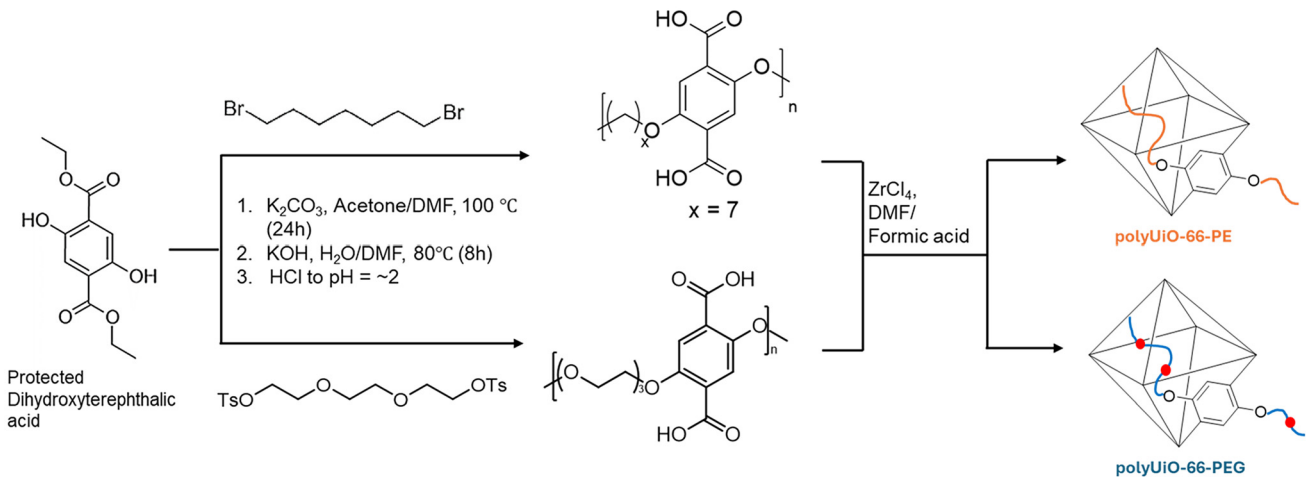

Scheme 1 General reaction scheme for polylinker synthesis.

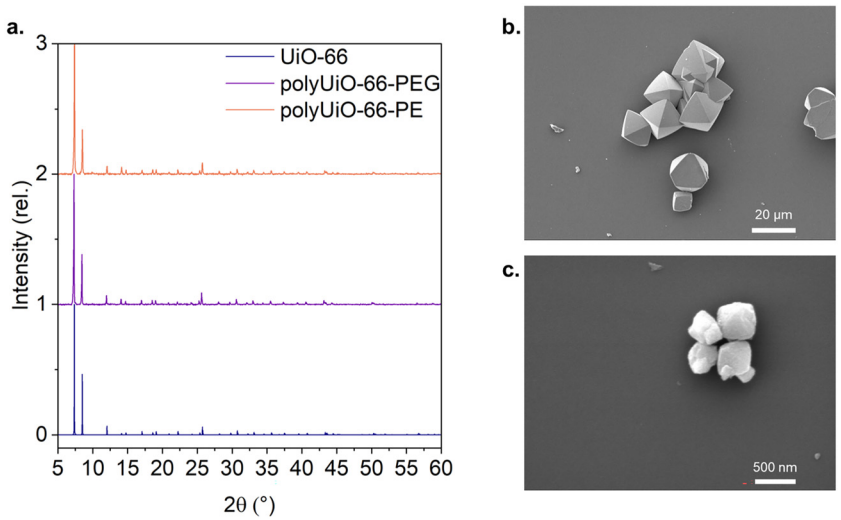

Fig. 1 (a) Powder X-ray diffraction for UiO-66-PE (orange), UiO-66-PEG (purple), and UiO-66 (simulated, blue). SEM image of (b) UiO-66-PEG and (c) UiO-66-PE, showing intergrown particles.

Fig. 1b and c, respectively. For polyUiO-66-PEG, 10–20 μm octahedral crystals are observed with some intergrown particles.[48,49] Conversely, polyUiO-66-PE particles are octahedral with widths that range from 0.5–2 μm. Additional SEM images can be found in the SI (Fig. S4). Thermogravimetric analysis (TGA) was used to determine decomposition temperature, with both polyMOFs seeing mass loss in the 300 °C–400 °C range (Fig. S5). The decomposition temperature is notably lower than that of unfunctionalized UiO-66, where major mass loss occurs around 500 °C.[50]

We next evaluated the ion transport properties of both polyMOFs. The powders of the polyMOFs were soaked in a propylene carbonate (PC) solution containing 1.0 M of $LiClO_4$. This step infiltrated the polyMOFs with liquid electrolyte, improving ion conduction while also improving safety and processability over liquid electrolyte systems.[51,52] Utilizing TGA and atomic absorption spectroscopy (AAS), we determined the PC and Li content in each of our MOF samples (Fig. S5 and Table S1) using a method outlined in the SI. The number of PC molecules per repeating molecular unit of polyUiO-66-PE and polyUiO-66-PEG after soaking in 1.0 M $LiClO_4$ in PC is determined to be 7.62 and 8.27, respectively, resulting in estimated empirical formulas of $Zr_6O_4(OH)_4$(pbdc-7pe)$_6$(PC)$_{7.62}$($LiClO_4$)$_{9.39}$ and $Zr_6O_4(OH)_4$(pbdc-8peg)$_6$(PC)$_{8.27}$($LiClO_4$)$_{9.45}$. After vacuum filtration and drying in an Ar glovebox, the powders were pressed into a pellet in a custom-built die. The room-temperature ionic conductivity of the pressed pellets was calculated using the equation $\sigma = l/RA$, where σ is ionic conductivity, l is the thickness of the sample pellet, R is the resistance determined from electrochemical impedance spectroscopy (EIS, Table 1), and A is the contact area. The fit of the Nyquist plot was based on the equivalent

circuit shown in Fig. 2a, where R_1 is the uncompensated resistance, R_2 is the intra-grain resistance, and R_3 is the grain boundary resistance, while Q and W elements represent constant phase element capacitance and Warburg diffusion, respectively.[53] Higher frequency impedance contributions are said to be associated with grain resistance, while lower frequency impedance contributions are ascribed to grain boundary resistance.[54]

Notably, polyUiO-66-PEG had a lower total resistance (R_{total}) and higher total ionic conductivity (σ_{total}) compared to polyUiO-66-PE, as denoted in Table 1. To compare to a non-functionalized version, we also ran EIS of a sample of UiO-66 loaded with our PC/$LiClO_4$ solution and observed both polyMOFs exhibit superior total ionic conductivity compared to the parent UiO-66 (Fig. S6). Table S2 is offered for comparison of other MOF-based QSSEs and MOF–polymer composites. We hypothesize the lower intra-grain resistance of polyUiO-66-PEG (R_2 = 19.46 kΩ cm^{-1}, σ_{grain} = 1.82 × 10^{-4} S cm^{-1}) compared to that of polyUiO-66-PE (R_2 = 55.55 kΩ cm^{-1}, σ_{grain} = 6.37 × 10^{-5} S cm^{-1}) is due to the polar oxide group in PEG that allows for Li^+ coordination, serving as anchoring points as Li^+ travels through the material. Additionally, the grain boundary contribution for resistance of polyUiO-66-PEG (R_3 = 29.34 kΩ cm^{-1}) is lower than that of polyUiO-66-PEG (R_3 = 62.18 kΩ cm^{-1}), which has been previously attributed to the difference in particle size in other solid-state electrolyte candidates.[55] Based on SEM, polyUiO-66-PEG particles tend to be larger than polyUiO-66-PE particles, which likely contributes to its lower grain boundary resistance. Unfortunately, size control of polyMOFs has not been accomplished at this time.

At varying temperatures, the conductivities of the polyMOF electrolytes exhibited Arrhenius-like behavior as seen in Fig. 2, allowing for calculation of the activation energy through the slope of a linearized Arrhenius plot. The activation energy for Li^+ conductivity for polyUiO-66-PEG and polyUiO-66-PE was 0.19 eV and 0.24 eV, respectively, which is significantly lower than reported activation energies for PEG/LiTFSI electrolytes (0.38–0.43 eV).[56] Additionally, the functionalization of UiO-66 with copolymerized PEG shows an improvement in the activation energy over previously reported unfunctionalized UiO-66 infiltrated with Li^+ in a similar fashion with a reported value of 0.21 eV.[24] We also note that the Arrhenius plot only show a single linear trend for polyUiO-66-PEG, whereas two regimes representing conduction pathways through the crystalline and amorphous phases are identified in solid-state PEG electrolytes.[57]

We also compared our polyMOF electrolytes based on Li^+ transference number (t_{Li^+}), which is defined as the fraction of the total electric current carried in an electrolyte by Li^+.[58] The value of t_{Li^+} is equal to 1 in an ideal Li^+-conducting electrolyte; a t_{Li^+} < 1 typically indicates anion mobility. Utilizing the Bruce–Vincent method[36,37] on a symmetric Li|polyMOF|Li cell (Fig. 3 and Fig. S7), we determined t_{Li^+} to be 0.81 and 0.44 for Li-loaded polyUiO-66-PEG and polyUiO-66-PE, respectively, at 25 °C. The high transference number of polyUiO-66-PEG compared to those of polyUiO-66-PE and parent UiO-66[24,59] highlights the important role of the polar oxidic sites in the PEG units.[24,59] Remarkably, the transference numbers of both polyMOFs are above the value of 0.2 for PEG/LiTFSI solid-state electrolyte at room temperature,[60] which suggest the structure and porosity of polyMOF may impede anion diffusion as postulated by prior studies.[61,62] We acknowledge that the Bruce–Vincent method necessitates key assumptions, such an ideal dilute solution and negligible ion-pair association; we thus use t_{Li^+} for comparison purposes between similar materials, rather than an absolute measure.[63–66]

We also employed solid-state ^{7}Li NMR spectroscopy to observe changes to the local Li environment as a function of temperature (Fig. 4). In polyUiO-66-PEG, a broad feature at −0.63 ppm narrows as the temperature increases from −30 °C to 70 °C, whereas the dominant Li^+ peak maintains its shape in both polyUiO-66-PE and parent UiO-66 (Fig. S8). We speculate the broad feature seen in polyUiO-66-PEG is due to slow Li^+ exchange as Li^+ coordinates strongly to the oxidic groups in the PEG units at low temperatures, a phenomenon that has also been observed for PEG-based solid polymer electrolyte.[67] Using the Hendrickson and Bray equation (eqn (S3)),[38] we calculated the local activation energy for Li^+ hopping to be 0.10 eV, which is lower than the literature values of PEG electrolyte.[67,68] Based on our data, we postulate the oxide sites on the polymer linker of UiO-66-PEG play a key role in the improved Li^+ conductivity. Due to the often difficult-to-deconvolute interactions between solvent, ions, and framework, experimentally determining exact Li^+ transport mechanism can be challenging and therefore we turn into DFT calculations to understand the interplay between the solvent, polylinker, and secondary building unit (SBU) of MOF for dictating Li^+ transport behavior.

It is shown from DFT-relaxed polyUiO-66-PEG structures (Fig. 5a and b) that the polymer chains predominantly occupy the octahedral pores within the polyUiO-66-PEG MOF framework. The polymer chains can connect between the 1,4-benze-

Table 1 Room-temperature (25 °C) resistances and ionic conductivities of polyMOF and control pellets

	R_2 (kΩ cm^{-1})	R_3 (kΩ cm^{-1})	R_{total} (kΩ cm^{-1})[a]	σ_{grain} (S cm^{-1})	σ_{total} (S cm^{-1})
PolyUiO-66-PE	55.55	62.18	117.7	6.37 × 10^{-5}	3.005 × 10^{-5}
PolyUiO-66-PEG	19.46	29.34	48.80	1.82 × 10^{-4}	7.248 × 10^{-5}
UiO-66	225.8	198.4	424.2	1.25 × 10^{-6}	8.339 × 10^{-6}

[a] R_{total} is calculated from the sum of intra-grain resistance (R_2) and grain boundary resistance (R_3). R_1 (uncompensated resistance) has a negligible contribution to R_{total} and is therefore omitted. All resistance values are normalized by thickness of the pellet.

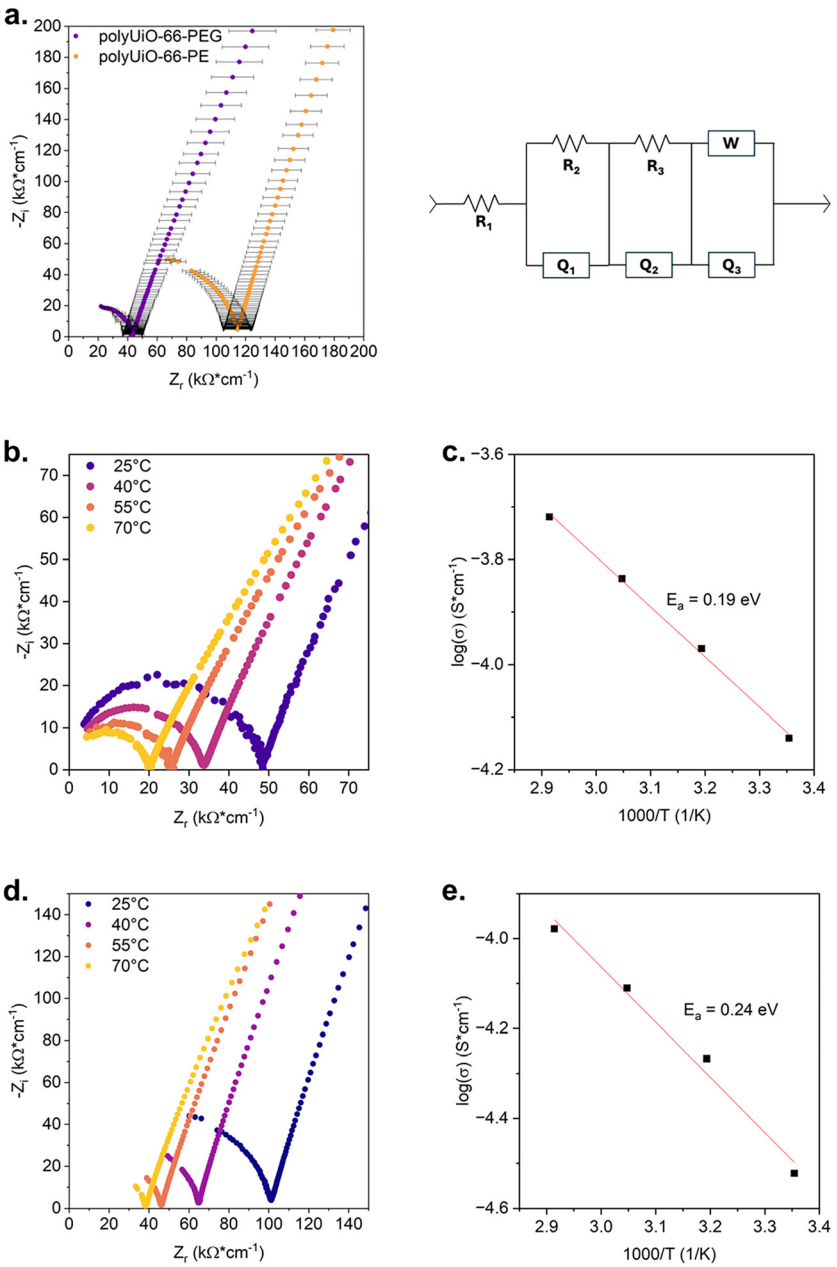

Fig. 2 (a) Room temperature (25 °C) Nyquist plots of polyUiO-66-PEG (purple) and polyUiO-66-PE (orange), showing average data from triplicate cells, and associated equivalent circuit fit. VT-EIS and Arrhenius plot for (b and c) polyUiO-66-PEG and (d and e) polyUiO-66-PE.

nedicarboxylate linkers in different conformations, rendering either a slack or taut configuration.[69] Accordingly, two distinct polyUiO-66-PEG configurations (denoted as "short" and "long" arrangements based on their intermolecular distances) were tested in this work and their relative formation energies are compared in Fig. 5c. Using a unit cell representation of UiO-66, combination of possible "short" and "long" configurations of PEG were also tested to determine the lowest energy configuration for subsequent studies. As shown in Fig. 5c, DFT relaxation suggests the "all short" configuration is energetically most favorable and thus was chosen as a model system to study Li^+ transport mechanism in PEG-functionalized UiO-66 polyMOF.

As shown in Fig. 6a and Fig. S9, a viable Li^+ conduction pathway is identified, featuring Li^+ migration through the tetrahedral and octahedral pores within the polyUiO-66-PEG structure. The relative energies of favorable Li^+ adsorption at specific local atomic sites along its migration pathway is calculated using DFT and the results are compared in Fig. 6a (black line). The associated change of local coordination environment of Li^+ during migration is further analyzed and the results are presented in Fig. 6b. Starting with the larger tetra-

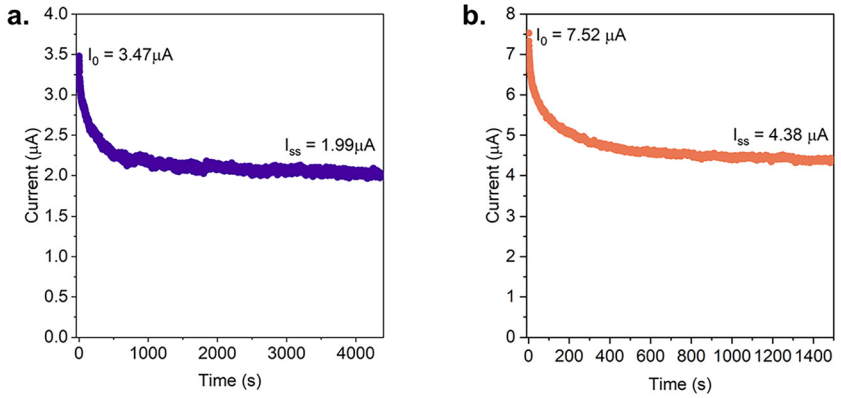

Fig. 3 Polarization of (a) polyUiO-66-PEG and (b) polyUiO-66-PE for Li-ion transference calculation.

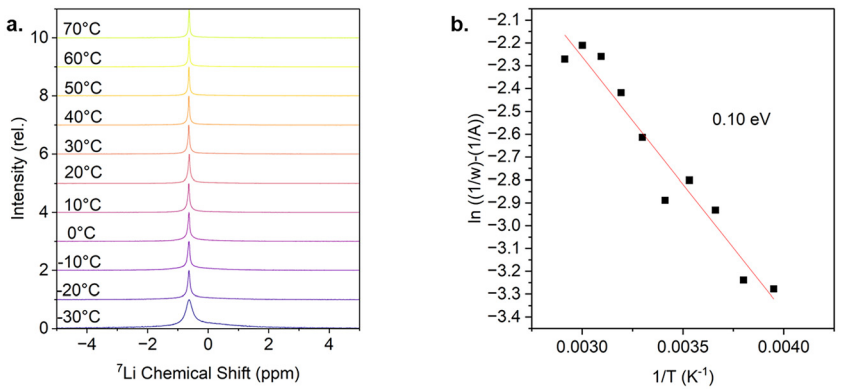

Fig. 4 (a) Solid-state ^{7}Li NMR spectroscopy of polyUiO-66-PEG at temperatures ranging from −30 °C to 70 °C, showing motional narrowing of the lithium peak. (b) Plot and calculated local activation energy for polyUiO-66-PEG from solid-state ^{7}Li NMR spectra and fitted to the Hendrickson and Bray equation.[26]

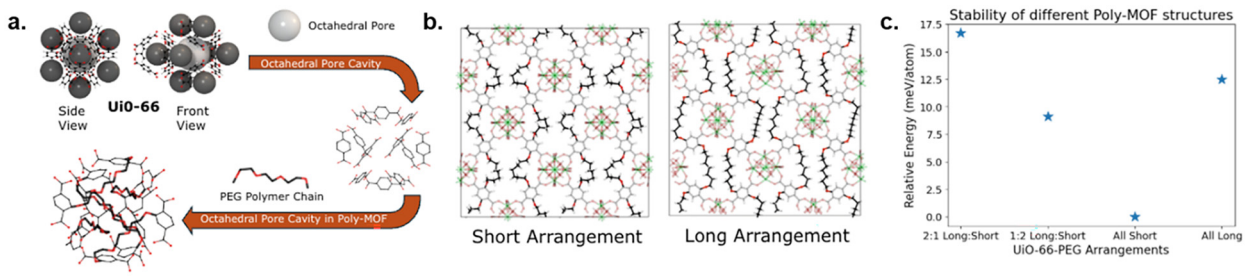

Fig. 5 (a) Representation of incorporating PEG polymer chain into the UiO-66 framework. (b) Schematic illustration of possible PEG chain arrangements inside UiO-66. (c) Relative stability of different UiO-66-PEG configurations based on a unit cell of UiO-66.

hedral pore (sites 0 and 1), Li^+ is preferably coordinated by both SBU and polymer linker in polyUiO-66-PEG, leading to local coordination number of 4 with an average Li–O distance of ~ 2 Å. When passing through the narrower octahedral pores, Li^+ becomes solely coordinated by the polymer chain as the pore is predominately filled by the polymer. To understand the effect of partial solvation, the calculation was repeated with the incorporation of an additional PC molecule along the Li^+ diffusion pathway. It is evidenced in Fig. 6a that the inclusion of a single PC molecule effectively revises the energy landscape of the metastable Li^+ adsorption at various local atomic sites within the polyUiO-66-PEG framework. More noticeably, the thermodynamic energy penalty to occupy the high-energy states (sites 2 and 3 in Fig. 6a) are significantly lowered in the presence of a PC molecule, implying potentially improved Li^+ transport kinetics across these sites.

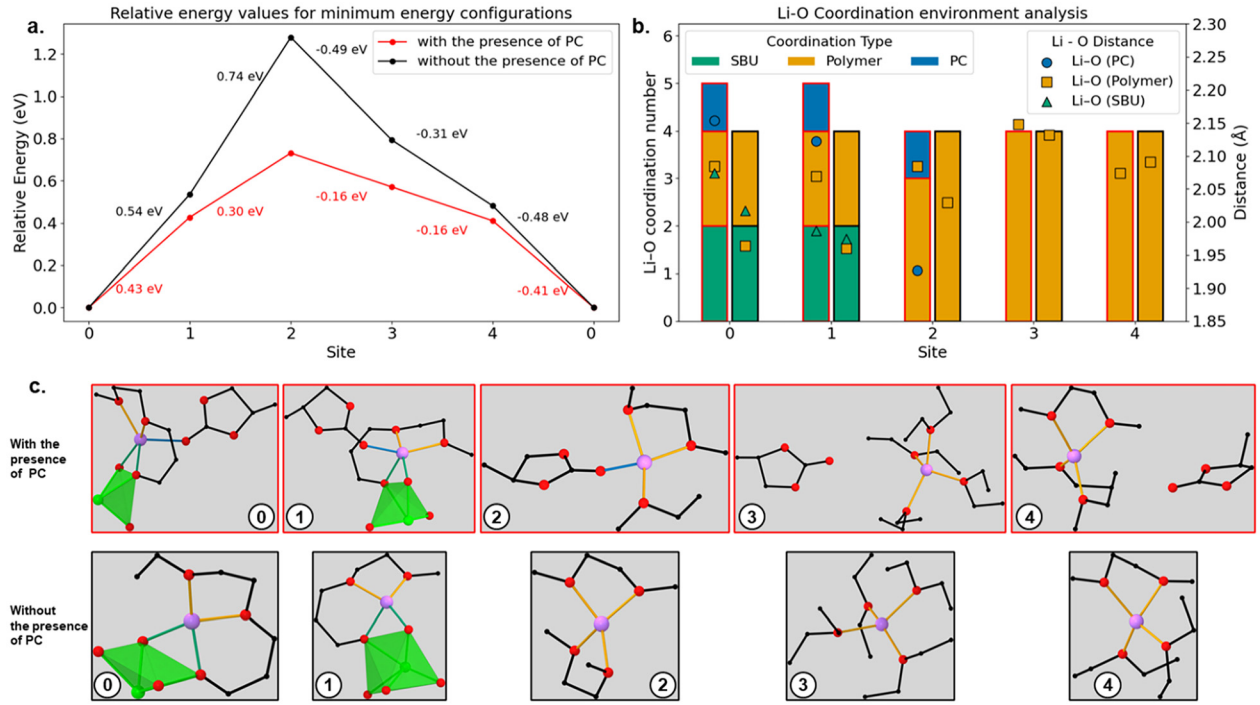

Fig. 6 (a) Relative energies of incorporating free Li^+ and partially solvated Li^+ at various sites within the polyUiO-66-PEG framework, scaled by the lowest adsorption energy at the tetrahedral site. (b) Corresponding analysis of the change of local Li coordination environment, described by Li–O coordination number (left) and average bond length (right), during Li^+ migration from the tetrahedral pore through the octahedral channel. The box line corresponds to the same color coding used in the line plot in panel (a) to depict the results of free Li^+ *vs.* single PC-coordinated Li^+ migration. (c) Schematic representations of minimum energy configurations at respective Li^+ adsorption sites. The Li–O bond colors are consistent with the coordination color scheme shown in panel (b).

Interestingly, closer examination of the local Li coordination environment shows the solvent molecule, PC in this case, can dynamically coordinate Li^+ within the tetrahedral and octahedral pores, and together with the PEG polylinker, create a thermodynamically favorable coordination environment for Li^+ diffusion. Here we emphasize the importance of the flexibility offered by PEG-functionalized UiO-66 polyMOF, to allow dynamical switching between PC and PEG coordination environment of Li^+, especially at sites 3 and 4 within the narrow octahedral pore, to facilitate its migration. As highlighted in Fig. S10a, when PC remains coordinating with Li^+ at these sites (3 and 4), the adsorption energies become substantially higher as compared to the cases where Li^+ is solely coordinated by the polymer chain. This observation strongly addresses the critical role of the competing effect of polymer linker and solvent molecule to coordinate Li^+ during migration within the polyUiO-66-PEG framework. In this regard, this solvent-mediated Li^+ transport mechanism may be generally relevant in functionalized polyMOFs, especially when the solvents and polymer linkers possess comparable coordination strength with Li^+.

Furthermore, pore size analysis reveals that the octahedral pore volume decreases significantly from 449.6 $Å^3$ in UiO-66 to 139 $Å^3$ in polyUiO-66-PEG. The irregular voids within the polymer matrix are sufficiently small to accommodate only mono-cation species with solvation radius of up to 2.3 Å. In contrast, the tetrahedral pore with a volume of 348 $Å^3$, which is larger than the octahedral pore, can host solvent molecules with solvation diameters ranging from 7.5 to 8 Å, such as dimethylsulfoxide, ethylene carbonate, DME, and DOL, as well as anions like FSI^-, PF_6^-, and BF_4^-. The $TFSI^-$ anion, however, with an effective radius of ~7.9 Å and multiple possible conformations may face steric hindrance and thus less likely to infiltrate the polyUiO-66-PEG structure.[70] Experimental data shows the significant change in the impedance of polyUiO-66-PEG when using a LiTFSI for infiltration (Fig. S12). These observation highlights the highly tunable nature of pore sizes within functionalized polyMOFs to selective transport cation species, such as Li^+ and Na^+, while limiting diffusion of larger anions, contact ion pairs and oligomers.

Conclusion

In summary, we have synthesized and characterized a novel UiO-66 polyMOF containing PEG units as a quasi-solid-state Li^+ conductor. Compared to the previously reported polyUiO-66-PE and parent UiO-66, polyUiO-66-PEG possesses a higher ionic conductivity and lower activation energy. Notably, the polymeric functionality has a dramatic impact on the Li transference number, with polyUiO-66-PEG significantly outperforming polyUiO-66-PE. The improved Li^+ transport pro-

perties suggest the oxidic group intrinsic to the polylinker of polyUiO-66-PEG plays a critical role in the Li^+ transport mechanism. PolyUiO-66-PEG also has an improved t_{Li^+} value compared to polyUiO-66-PE and solid-state NMR provides evidence of Li mobility, further supporting oxidic sites in the PEG unit is a major contributor to the improved ionic conductivity. DFT studies substantiate the critical role of these oxidic sites in PEG to coordinate Li^+ during its migration through the tetrahedral and octahedral pores of UiO-66. More importantly, DFT results reveal a confined, solvent-mediated quasi-solid-state Li^+ transport mechanism in PEG-functionalized UiO-66 framework, enabled by dynamical switching of Li^+ coordination environment between the solvent and polylinker. To conclude, our study illustrates the vast potential for polyMOFs and other framework materials to be versatile platforms for understanding ion conduction, paving the road for next-generation inorganic-polymer electrolytes for solid-state energy storage technologies.

Conflicts of interest

There are no conflicts to declare.

Data availability

Data for this article, including materials characterization, calculations, and electrochemical data are available at Johns Hopkins Data Repository at **https://doi.org/10.7281/T1RR968K**.

Supplementary information (SI) is available. See DOI: **https://doi.org/10.1039/d5qi02453f**.

Acknowledgements

This study is funded by the National Science Foundation (DMR-2532514) and the NSF CAREER Award (DMR-1945114). I. J. D. and R. Y. H. were partially supported by the Department of Chemistry at Johns Hopkins University through the Zeltman Graduate Research Fellowship and the Greer Undergraduate Research Fellowship, respectively. The computational portion of the work was performed under the auspices of the U. S. Department of Energy by Lawrence Livermore National Laboratory under contract DE-AC52-07NA27344. Funding support and part of the computational resource was provided by Laboratory Directed Research and Development funding under Projects 25-ERD-008. Additional computational support was provided by the U.S. Department of Energy's Office of Critical Minerals and Energy Innovation and located at the National Laboratory of the Rockies. We thank Dr Rebekka Klausen and Mr Brady Mediavilla for their assistance with GPC measurements, Prof. Regina Garcia-Mendez for insightful discussions on EIS analysis, Prof. Yuting Luo for advice on electrochemical measurements, Dr Kyle Barcus for his synthetic advice and assistance in SEM, and Dr Jonathan Catazaro for NMR assistance. We are also grateful for the support from the Ralph O'Connor Sustainable Energy Institute and the Camille and Henry Dreyfus Foundation.

References

1 L. Han, L. Wang, Z. Chen, Y. Kan, Y. Hu, H. Zhang and X. He, Incombustible Polymer Electrolyte Boosting Safety of Solid-State Lithium Batteries: A Review, *Adv. Funct. Mater.*, 2023, **33**(32), 2300892, DOI: **10.1002/adfm.202300892**.

2 H.-D. Lim, J.-H. Park, H.-J. Shin, J. Jeong, J. T. Kim, K.-W. Nam, H.-G. Jung and K. Y. Chung, A Review of Challenges and Issues Concerning Interfaces for All-Solid-State Batteries, *Energy Storage Mater.*, 2020, **25**, 224–250, DOI: **10.1016/j.ensm.2019.10.011**.

3 Z. Moradi, A. Lanjan, R. Tyagi and S. Srinivasan, Review on Current State, Challenges, and Potential Solutions in Solid-State Batteries Research, *J. Energy Storage*, 2023, **73**, 109048, DOI: **10.1016/j.est.2023.109048**.

4 M. Ma, M. Zhang, B. Jiang, Y. Du, B. Hu and C. Sun, A Review of All-Solid-State Electrolytes for Lithium Batteries: High-Voltage Cathode Materials, Solid-State Electrolytes and Electrode–Electrolyte Interfaces, *Mater. Chem. Front.*, 2023, **7**(7), 1268–1297, DOI: **10.1039/D2QM01071B**.

5 J. Janek and W. G. Zeier, Challenges in Speeding up Solid-State Battery Development, *Nat. Energy*, 2023, **8**(3), 230–240, DOI: **10.1038/s41560-023-01208-9**.

6 S. Jian, Y. Cao, W. Feng, G. Yin, Y. Zhao, Y. Lai, T. Zhang, X. Ling, H. Wu, H. Bi and Y. Dong, Recent Progress in Solid Polymer Electrolytes with Various Dimensional Fillers: A Review, *Mater. Today Sustain.*, 2022, **20**, 100224, DOI: **10.1016/j.mtsust.2022.100224**.

7 Z. Song, F. Chen, M. Martinez-Ibañez, W. Feng, M. Forsyth, Z. Zhou, M. Armand and H. Zhang, A Reflection on Polymer Electrolytes for Solid-State Lithium Metal Batteries, *Nat. Commun.*, 2023, **14**(1), 4884, DOI: **10.1038/s41467-023-40609-y**.

8 P. Yao, H. Yu, Z. Ding, Y. Liu, J. Lu, M. Lavorgna, J. Wu and X. Liu, Review on Polymer-Based Composite Electrolytes for Lithium Batteries, *Front. Chem.*, 2019, **7**, 522, DOI: **10.3389/fchem.2019.00522**.

9 X. Zhao, C. Wang, H. Liu, Y. Liang and L.-Z. Fan, A Review of Polymer-Based Solid-State Electrolytes for Lithium-Metal Batteries: Structure, Kinetic, Interface Stability, and Application, *Batteries Supercaps*, 2023, **6**(4), e202200502, DOI: **10.1002/batt.202200502**.

10 D. Karabelli, K. P. Birke and M. Weeber, A Performance and Cost Overview of Selected Solid-State Electrolytes: Race between Polymer Electrolytes and Inorganic Sulfide Electrolytes, *Batteries*, 2021, **7**(1), 18, DOI: **10.3390/batteries7010018**.

11 S. Hong, Y. Wang, N. Kim and S. B. Lee, Polymer-Based Electrolytes for All-Solid-State Lithium–Sulfur Batteries: From Fundamental Research to Performance Improvement, *J. Mater. Sci.*, 2021, **56**(14), 8358–8382, DOI: **10.1007/s10853-021-05832-2**.

12 N. H. A. M. Hashim and R. H. Y. Subban, Studies on Conductivity, Structural and Thermal Properties of PEO-LiTFSI Polymer Electrolytes Doped with EMImTFSI Ionic Liquid, *AIP Conf. Proc.*, 2018, **2031**((1)), 020021. DOI: 10.1063/1.5066977.

13 T. I. Kolesnikov, D. Voll, F. Jeschull and P. Theato, Synthesis of Polyimide-PEO Copolymers: Toward Thermally Stable Solid Polymer Electrolytes for Lithium-Metal Batteries, *Eur. Polym. J.*, 2024, **217**, 113315, DOI: 10.1016/j.eurpolymj.2024.113315.

14 M. U. Javed, S. Muhammad, Z. Wang, J. Li, X. Wu, A. Chukwuka, Y. Zhang, K. Wang and B. Guo, Metal-Organic Framework/Polymer Composites for Solid State Electrolytes-A Critical Review, *J. Power Sources*, 2025, **640**, 236720, DOI: 10.1016/j.jpowsour.2025.236720.

15 Q. Zhou, J. Ma, S. Dong, X. Li and G. Cui, Intermolecular Chemistry in Solid Polymer Electrolytes for High-Energy-Density Lithium Batteries, *Adv. Mater.*, 2019, **31**(50), 1902029, DOI: 10.1002/adma.201902029.

16 Introduction to Metal–Organic Frameworks, *Chem. Rev.*, 2012, **112**(2), 673–674, DOI: 10.1021/cr300014x.

17 R. Zhao, Z. Liang, R. Zou and Q. Xu, Metal-Organic Frameworks for Batteries, *Joule*, 2018, **2**(11), 2235–2259, DOI: 10.1016/j.joule.2018.09.019.

18 P. Dong, X. Zhang, W. Hiscox, J. Liu, J. Zamora, X. Li, M. Su, Q. Zhang, X. Guo, J. McCloy and M.-K. Song, Toward High-Performance Metal–Organic-Framework-Based Quasi-Solid-State Electrolytes: Tunable Structures and Electrochemical Properties, *Adv. Mater.*, 2023, **35**(32), 2211841, DOI: 10.1002/adma.202211841.

19 X. Judez, M. Martinez-Ibañez, A. Santiago, M. Armand, H. Zhang and C. Li, Quasi-Solid-State Electrolytes for Lithium Sulfur Batteries: Advances and Perspectives, *J. Power Sources*, 2019, **438**, 226985, DOI: 10.1016/j.jpowsour.2019.226985.

20 X. Judez, M. Martinez-Ibañez, A. Santiago, M. Armand, H. Zhang and C. Li, Quasi-Solid-State Electrolytes for Lithium Sulfur Batteries: Advances and Perspectives, *J. Power Sources*, 2019, **438**, 226985, DOI: 10.1016/j.jpowsour.2019.226985.

21 J. Liu, Y. Wu, Z. Chen, Z. Xu, J. Zhu and X. Zhuang, In Situ Polymerization-Driven Quasi-Solid Electrolytes for Li-Metal Batteries, *Mater. Chem. Front.*, 2025, **9**(13), 1971–1996, DOI: 10.1039/D5QM00116A.

22 R. A. Kharod, J. L. Andrews and M. Dincă, Teaching Metal-Organic Frameworks to Conduct: Ion and Electron Transport in Metal-Organic Frameworks, *Annu. Rev. Mater. Res.*, 2022, **52**, 103–128, DOI: 10.1146/annurev-matsci-080619-012811.

23 T. Hou and W. Xu, Deep Dive into Anionic Metal-Organic Frameworks Based Quasi-Solid-State Electrolytes, *J. Energy Chem.*, 2023, **81**, 313–320, DOI: 10.1016/j.jechem.2023.02.048.

24 L. Shen, H. B. Wu, F. Liu, J. L. Brosmer, G. Shen, X. Wang, J. I. Zink, Q. Xiao, M. Cai, G. Wang, Y. Lu and B. Dunn, Creating Lithium-Ion Electrolytes with Biomimetic Ionic Channels in Metal–Organic Frameworks, *Adv. Mater.*, 2018, **30**(23), 1707476, DOI: 10.1002/adma.201707476.

25 C. Zhang, L. Shen, J. Shen, F. Liu, G. Chen, R. Tao, S. Ma, Y. Peng and Y. Lu, Anion-Sorbent Composite Separators for High-Rate Lithium-Ion Batteries, *Adv. Mater.*, 2019, **31**(21), 1808338, DOI: 10.1002/adma.201808338.

26 M. U. Javed, S. Muhammad, Z. Wang, J. Li, X. Wu, A. Chukwuka, Y. Zhang, K. Wang and B. Guo, Metal-Organic Framework/Polymer Composites for Solid State Electrolytes-A Critical Review, *J. Power Sources*, 2025, **640**, 236720, DOI: 10.1016/j.jpowsour.2025.236720.

27 N. Angulakshmi, Y. Zhou, S. Suriyakumar, R. B. Dhanalakshmi, M. Satishrajan, S. Alwarappan, M. H. Alkordi and A. M. Stephan, Microporous Metal–Organic Framework (MOF)-Based Composite Polymer Electrolyte (CPE) Mitigating Lithium Dendrite Formation in All-Solid-State-Lithium Batteries, *ACS Omega*, 2020, **5**(14), 7885–7894, DOI: 10.1021/acsomega.9b04133.

28 S. Duan, L. Qian, Y. Zheng, Y. Zhu, X. Liu, L. Dong, W. Yan and J. Zhang, Mechanisms of the Accelerated Li+ Conduction in MOF-Based Solid-State Polymer Electrolytes for All-Solid-State Lithium Metal Batteries, *Adv. Mater.*, 2024, **36**(32), 2314120, DOI: 10.1002/adma.202314120.

29 H. Wang, S. Duan, Y. Zheng, L. Qian, C. Liao, L. Dong, H. Guo, C. Ma, W. Yan and J. Zhang, Solid-State Electrolytes Based on Metal-Organic Frameworks for Enabling High-Performance Lithium-Metal Batteries: Fundamentals, Progress, and Perspectives, *eTransportation*, 2024, **20**, 100311, DOI: 10.1016/j.etran.2024.100311.

30 Z. Zhang, H. T. H. Nguyen, S. A. Miller and S. M. Cohen, polyMOFs: A Class of Interconvertible Polymer-Metal-Organic-Framework Hybrid Materials, *Angew. Chem., Int. Ed.*, 2015, **54**(21), 6152–6157, DOI: 10.1002/anie.201502733.

31 K. C. Bentz, K. Gnanasekaran, J. B. Bailey, S. Ayala, F. A. Tezcan, N. C. Gianneschi and S. M. Cohen, Inside polyMOFs: Layered Structures in Polymer-Based Metal–Organic Frameworks, *Chem. Sci.*, 2020, **11**(38), 10523–10528, DOI: 10.1039/D0SC03651J.

32 Z. Zhang, H. T. H. Nguyen, S. A. Miller, A. M. Ploskonka, J. B. DeCoste and S. M. Cohen, Polymer–Metal–Organic Frameworks (polyMOFs) as Water Tolerant Materials for Selective Carbon Dioxide Separations, *J. Am. Chem. Soc.*, 2016, **138**(3), 920–925, DOI: 10.1021/jacs.5b11034.

33 M. Kalaj, K. C. Bentz, S. Ayala Jr., J. M. Palomba, K. S. Barcus, Y. Katayama and S. M. Cohen, MOF-Polymer Hybrid Materials: From Simple Composites to Tailored Architectures, *Chem. Rev.*, 2020, **120**(16), 8267–8302, DOI: 10.1021/acs.chemrev.9b00575.

34 P. Duan, J. C. Moreton, S. R. Tavares, R. Semino, G. Maurin, S. M. Cohen and K. Schmidt-Rohr, Polymer Infiltration into Metal–Organic Frameworks in Mixed-Matrix Membranes Detected in Situ by NMR, *J. Am. Chem. Soc.*, 2019, **141**(18), 7589–7595, DOI: 10.1021/jacs.9b02789.

35 S. Ayala, Z. Zhang and S. M. Cohen, Hierarchical Structure and Porosity in UiO-66 polyMOFs, *Chem. Commun.*, 2017, **53**(21), 3058–3061, DOI: 10.1039/C6CC10225E.

36 J. Evans, C. A. Vincent and P. G. Bruce, Electrochemical Measurement of Transference Numbers in Polymer Electrolytes, *Polymer*, 1987, **28**(13), 2324–2328, DOI: 10.1016/0032-3861(87)90394-6.

37 P. G. Bruce and C. A. Vincent, Steady State Current Flow in Solid Binary Electrolyte Cells, *J. Electroanal. Chem. Interfacial Electrochem.*, 1987, **225**(1), 1–17, DOI: 10.1016/0022-0728(87)80001-3.

38 J. R. Hendrickson and P. J. Bray, A Phenomenological Equation for NMR Motional Narrowing in Solids, *J. Magn. Reson.*, 1973, **9**(3), 341–357, DOI: 10.1016/0022-2364(73)90176-5.

39 A. U. Mu, V. V. Singh, H. Kim, D. J. Lee, N. Kim, C. X. Ruff, A. Levy, T. A. Young, F. Paesani, S. M. Cohen, T. A. Pascal and Z. Chen, Structure–Activity Relationships in Ether-Functionalized Solid-State Metal–Organic Framework Electrolytes, *Chem. Mater.*, 2025, **37**(8), 2783–2794, DOI: 10.1021/acs.chemmater.4c03384.

40 A. K. Rappe, C. J. Casewit, K. S. Colwell, W. A. I. Goddard and W. M. Skiff, UFF, a Full Periodic Table Force Field for Molecular Mechanics and Molecular Dynamics Simulations, *J. Am. Chem. Soc.*, 1992, **114**(25), 10024–10035, DOI: 10.1021/ja00051a040.

41 A. V. Marenich, S. V. Jerome, C. J. Cramer and D. G. Truhlar, Charge Model 5: An Extension of Hirshfeld Population Analysis for the Accurate Description of Molecular Interactions in Gaseous and Condensed Phases, *J. Chem. Theory Comput.*, 2012, **8**(2), 527–541, DOI: 10.1021/ct200866d.

42 T. Hou, W. Xu, X. Pei, L. Jiang, O. M. Yaghi and K. A. Persson, Ionic Conduction Mechanism and Design of Metal–Organic Framework Based Quasi-Solid-State Electrolytes, *J. Am. Chem. Soc.*, 2022, **144**(30), 13446–13450, DOI: 10.1021/jacs.2c03710.

43 G. Kresse and J. Furthmüller, Efficient Iterative Schemes for Ab Initio Total-Energy Calculations Using a Plane-Wave Basis Set, *Phys. Rev. B:Condens. Matter Mater. Phys.*, 1996, **54**(16), 11169–11186, DOI: 10.1103/PhysRevB.54.11169.

44 P. E. Blöchl, Projector Augmented-Wave Method, *Phys. Rev. B:Condens. Matter Mater. Phys.*, 1994, **50**(24), 17953–17979, DOI: 10.1103/PhysRevB.50.17953.

45 J. P. Perdew, K. Burke and M. Ernzerhof, Generalized Gradient Approximation Made Simple, *Phys. Rev. Lett.*, 1996, 77(18), 3865–3868, DOI: 10.1103/PhysRevLett.77.3865.

46 C. F. Macrae, I. Sovago, S. J. Cottrell, P. T. A. Galek, P. McCabe, E. Pidcock, M. Platings, G. P. Shields, J. S. Stevens, M. Towler and P. A. Wood, Mercury 4.0: From Visualization to Analysis, Design and Prediction, *J. Appl. Crystallogr.*, 2020, **53**(1), 226–235, DOI: 10.1107/S1600576719014092.

47 M. Eddaoudi, H. Li, T. Reineke, M. Fehr, D. Kelley, T. L. Groy and O. M. Yaghi, Design and Synthesis of Metal-Carboxylate Frameworks with Permanent Microporosity, *Top. Catal.*, 1999, **9**(1), 105–111, DOI: 10.1023/A:1019110622091.

48 B. Gibbons, E. C. Bartlett, M. Cai, X. Yang, E. M. Johnson and A. J. Morris, Defect Level and Particle Size Effects on the Hydrolysis of a Chemical Warfare Agent Simulant by UiO-66, *Inorg. Chem.*, 2021, **60**(21), 16378–16387, DOI: 10.1021/acs.inorgchem.1c02224.

49 K. Y. Cho, J. Y. Seo, H.-J. Kim, S. J. Pai, X. H. Do, H. G. Yoon, S. S. Hwang, S. S. Han and K.-Y. Baek, Facile Control of Defect Site Density and Particle Size of UiO-66 for Enhanced Hydrolysis Rates: Insights into Feasibility of Zr(IV)-Based Metal-Organic Framework (MOF) Catalysts, *Appl. Catal., B*, 2019, **245**, 635–647, DOI: 10.1016/j.apcatb.2019.01.033.

50 M. Athar, P. Rzepka, D. Thoeny, M. Ranocchiari and J. A. van Bokhoven, Thermal Degradation of Defective High-Surface-Area UiO-66 in Different Gaseous Environments, *RSC Adv.*, 2021, **11**(61), 38849–38855, DOI: 10.1039/D1RA05411B.

51 H. Liu, H. Pan, M. Yan, X. Zhang and Y. Jiang, Extraordinary Ionic Conductivity Excited by Hierarchical Ion-Transport Pathways in MOF-Based Quasi-Solid Electrolytes, *Adv. Mater.*, 2023, **35**(26), 2300888, DOI: 10.1002/adma.202300888.

52 X. Judez, M. Martinez-Ibañez, A. Santiago, M. Armand, H. Zhang and C. Li, Quasi-Solid-State Electrolytes for Lithium Sulfur Batteries: Advances and Perspectives, *J. Power Sources*, 2019, **438**, 226985, DOI: 10.1016/j.jpowsour.2019.226985.

53 P. Vadhva, J. Hu, M. J. Johnson, R. Stocker, M. Braglia, D. J. L. Brett and A. J. E. Rettie, Electrochemical Impedance Spectroscopy for All-Solid-State Batteries: Theory, Methods and Future Outlook, *ChemElectroChem*, 2021, **8**(11), 1930–1947, DOI: 10.1002/celc.202100108.

54 J. T. S. Irvine, D. C. Sinclair and A. R. West, Electroceramics: Characterization by Impedance Spectroscopy, *Adv. Mater.*, 1990, **2**(3), 132–138, DOI: 10.1002/adma.19900020304.

55 E. Milan and M. Pasta, The Role of Grain Boundaries in Solid-State Li-Metal Batteries, *Mater. Futures*, 2022, **2**(1), 013501, DOI: 10.1088/2752-5724/aca703.

56 D. J. Brooks, B. V. Merinov, W. A. I. Goddard, B. Kozinsky and J. Mailoa, Atomistic Description of Ionic Diffusion in PEO–LiTFSI: Effect of Temperature, Molecular Weight, and Ionic Concentration, *Macromolecules*, 2018, **51**(21), 8987–8995, DOI: 10.1021/acs.macromol.8b01753.

57 V. St-Onge, M. Cui, S. Rochon, J.-C. Daigle and J. P. Claverie, Reducing Crystallinity in Solid Polymer Electrolytes for Lithium-Metal Batteries via Statistical Copolymerization, *Commun. Mater.*, 2021, **2**(1), 1–11, DOI: 10.1038/s43246-021-00187-2.

58 K. D. Fong, J. Self, K. M. Diederichsen, B. M. Wood, B. D. McCloskey and K. A. Persson, Ion Transport and the True Transference Number in Nonaqueous Polyelectrolyte Solutions for Lithium Ion Batteries, *ACS Cent. Sci.*, 2019, **5**(7), 1250–1260, DOI: 10.1021/acscentsci.9b00406.

59 J. Yang, L. Shao, X. Wang, Y. Yang, Z. Tian, W. Chen, G. Zhang and C. Shen, Effect of Intermolecular

Interactions on the Performance of UiO-66-Laden Solid Composite Polymer Electrolytes, *J. Alloys Compd.*, 2020, **845**, 155179, DOI: 10.1016/j.jallcom.2020.155179.

60 Y. Zhao, L. Wang, Y. Zhou, Z. Liang, N. Tavajohi, B. Li and T. Li, Solid Polymer Electrolytes with High Conductivity and Transference Number of Li Ions for Li-Based Rechargeable Batteries, *Adv. Sci.*, 2021, **8**(7), 2003675, DOI: 10.1002/advs.202003675.

61 Z. Wang, Z. Du, Y. Liu, C. E. Knapp, Y. Dai, J. Li, W. Zhang, R. Chen, F. Guo, W. Zong, X. Gao, J. Zhu, C. Wei and G. He, Metal–Organic Frameworks and Their Derivatives for Optimizing Lithium Metal Anodes, *eScience*, 2024, **4**(4), 100189, DOI: 10.1016/j.esci.2023.100189.

62 X. Hu, Q. Liu, K. Lin, C. Han and B. Li, The Rise of Metal–Organic Frameworks for Electrolyte Applications, *J. Mater. Chem. A*, 2021, **9**(37), 20837–20856, DOI: 10.1039/D1TA05201B.

63 L.-Y. Lin and C.-C. Chen, Accurate Characterization of Transference Numbers in Electrolyte Systems, *J. Power Sources*, 2024, **603**, 234236, DOI: 10.1016/j.jpowsour.2024.234236.

64 Y. Shao, H. Gudla, J. Mindemark, D. Brandell and C. Zhang, Ion Transport in Polymer Electrolytes: Building New Bridges between Experiment and Molecular Simulation, *Acc. Chem. Res.*, 2024, **57**(8), 1123–1134, DOI: 10.1021/acs.accounts.3c00791.

65 K. Xu, Navigating the Minefield of Battery Literature, *Commun. Mater.*, 2022, **3**(1), 31, DOI: 10.1038/s43246-022-00251-5.

66 D. M. Pesko, K. Timachova, R. Bhattacharya, M. C. Smith, I. Villaluenga, J. Newman and N. P. Balsara, Negative Transference Numbers in Poly(Ethylene Oxide)-Based Electrolytes, *J. Electrochem. Soc.*, 2017, **164**(11), E3569–E3575, DOI: 10.1149/2.0581711jes.

67 S. Zhang, L. F. Mueller, L. Macray, M. Wagemaker, L. J. Bannenberg and S. Ganapathy, Revealing Local Diffusion Dynamics in Hybrid Solid Electrolytes, *ACS Energy Lett.*, 2025, **10**(4), 1762–1771, DOI: 10.1021/acsenergylett.5c00214.

68 D.-W. Kim, J.-K. Park, H.-W. Rhee and H.-D. Kim, Ionic Conductivity and 7Li NMR Study of Solid Polymer Electrolytes Based on Polyetherurethane Copolymer Networks, *Polym. J.*, 1994, **26**(9), 993–1001, DOI: 10.1295/polymj.26.993.

69 P. G. M. Mileo, S. Yuan, S. Ayala Jr., P. Duan, R. Semino, S. M. Cohen, K. Schmidt-Rohr and G. Maurin, Structure of the Polymer Backbones in polyMOF Materials, *J. Am. Chem. Soc.*, 2020, **142**(24), 10863–10868, DOI: 10.1021/jacs.0c04546.

70 K. Fujii, T. Fujimori, T. Takamuku, R. Kanzaki, Y. Umebayashi and S. Ishiguro, Conformational Equilibrium of Bis(Trifluoromethanesulfonyl) Imide Anion of a Room-Temperature Ionic Liquid: Raman Spectroscopic Study and DFT Calculations, *J. Phys. Chem. B*, 2006, **110**(16), 8179–8183, DOI: 10.1021/jp0612477.